

Cite this: *Mater. Adv.*, 2022,  
3, 7107

# Interfacial engineering of Cu–Fe<sub>2</sub>O<sub>3</sub> nanotube arrays with built-in electric field and oxygen vacancies for boosting the electrocatalytic reduction of nitrates†

Yihong Gao,<sup>‡a</sup> Kun Huang,<sup>‡a</sup> Chen Yan,<sup>a</sup> Shikuo Li,<sup>\*b</sup> Hui Zhang,<sup>ib</sup> \*<sup>b</sup>  
Longjiu Cheng<sup>ib</sup> <sup>a</sup> and Fangzhi Huang<sup>ib</sup> \*<sup>a</sup>

The key to enhancing electrocatalytic nitrate reduction to ammonium (ENRA) is to improve the slow mass transfer of nitrates and the effective electron transfer on the catalyst surface. Based on the thermal diffusion theory and electroreduction mechanism, a Cu–Fe<sub>2</sub>O<sub>3</sub> nanotube electrocatalyst with enriched oxygen vacancies and a built-in electric field was designed by controlling the heating and electroreduction time. Because of its unique structure, it could induce the generation of a built-in electric field and promote the enrichment of nitrate ions and electron transfer on the catalyst surface. Combined with the oxygen vacancy (OV)-anchoring mechanism, Cu–Fe<sub>2</sub>O<sub>3</sub>-60 showed remarkable Faraday efficiency (80.1%) and selectivity (88.47%). In addition, even when the reactor was scaled up to a pilot capacity of 180 L, the conversion rate was close to 85%. This work demonstrates that controlling the staggered interface distribution and oxygen vacancy number in metal–semiconductor is an effective way to design high-efficiency electrocatalysts.

Received 14th June 2022,  
Accepted 19th July 2022

DOI: 10.1039/d2ma00685e

rsc.li/materials-advances

## 1. Introduction

Nitrate pollution is one of the most urgent environmental problems in the world, especially due to its accumulation in surface water and groundwater, seriously threatening human health.<sup>1–4</sup> The eight-electron transfer reaction of NO<sub>3</sub><sup>–</sup> conversion to NH<sub>4</sub><sup>+</sup> is employed not to partially reduce NO<sub>3</sub><sup>–</sup> into N<sub>2</sub> for purification but to provide an opportunity to convert polluting NO<sub>3</sub><sup>–</sup> into NH<sub>4</sub><sup>+</sup>, which is an economically competitive product.<sup>5,6</sup> Compared with the traditional commercial technologies,<sup>7–11</sup> the electrocatalytic technology is considered one of the most effective strategies for mitigating nitrate pollution due to its pollution-free process, low energy consumption and high energy efficiency.<sup>12–14</sup>

However, as an active but challenging field in current research, electrocatalysis also faces some inevitable difficulties. First, in the eight-electron transfer electrocatalytic nitrate reduction to ammonium, the main competitive side reaction

is the hydrogen evolution reaction, which is accompanied by a five-electron transfer reaction that partially reduces NO<sub>3</sub><sup>–</sup> to N<sub>2</sub>.<sup>15,16</sup> Moreover, the yield of ammonium also depends on solutions to key problems, such as the slow mass transfer of nitrate in solution, small concentration gradient near the electrode and weak anchoring on the catalyst surface.<sup>17,18</sup> In this scenario, the core of the technology lies in designing an integrated catalytic system to fully improve the catalytic performance.

As with any typical heterogeneous catalytic reaction, constructing heterogeneous interfaces between the constituent active components to achieve effective electron transfer is crucial in ENRA systems.<sup>19–22</sup> In metal–semiconductor electrocatalysts, the heterogeneous interface connects metals and a semiconductor; this structure, on the one hand, promotes efficient electron transport at the metal–semiconductor interface, and on the other hand, induces charge redistribution to affect the reactive activity.<sup>23–26</sup> Based on these advantages, we believe that this structure will achieve great ENRA performance. Metal–semiconductor electrocatalysts have indeed shown great potential in the ENRA field.<sup>27–29</sup> For example, Yu *et al.* prepared Co/CoO nanosheet arrays by a thermal reduction method, which utilized the rectification effect of Schottky contact between the metal and semiconductor to construct electron-deficient Co, thereby realizing selective electroreduction of nitrate to ammonium and turning waste into treasure.<sup>30</sup> Li *et al.* utilized the sulfur-diffusion method to construct high-

<sup>a</sup> Laboratory of Clean Energy & Environmental Catalysis, Anhui Province Key Laboratory of Chemistry for Inorganic/Organic Hybrid Functionalized Materials, School of Chemistry and Chemical Engineering, Anhui University, Hefei 230601, P. R. China. E-mail: huangfangzhi@163.com

<sup>b</sup> School of Materials Science and Engineering, Anhui University, Hefei 230601, P. R. China. E-mail: lishikuo@ahu.edu.cn, zhuhui@ahu.edu.cn; Tel: +86-551-63861328

† Electronic supplementary information (ESI) available. See DOI: <https://doi.org/10.1039/d2ma00685e>

‡ These authors contribute equally to this paper.

density Ni nanoparticles on nitrogen-rich carbon supports (Ni/NC), which promoted the enrichment and immobilization of all  $\text{NO}_x^-$  ions on the electrode surface, thereby ensuring the ultimate selectivity toward ammonia.<sup>31</sup> In addition, OV, the most basic form of defects, have been widely used in the ENRA field.<sup>32–35</sup> For example, OV in  $\text{TiO}_2$  can not only capture nitrate and weaken the N–O bond energy but also inhibit the generation of by-products, thus significantly improving the efficiency of electrocatalytic ammonia production.<sup>36</sup> OV in the amorphous  $\text{RuO}_2$  phase effectively regulate the d-band center and hydrogen affinity, thereby reducing the energy of the potential-determining step.<sup>37</sup> As we know, the electrochemical reduction of nitrates begins with its initial adsorption on the electrode surface ( $\text{NO}_3^-(\text{aq}) \rightleftharpoons \text{NO}_3^-(\text{ads})$ ).<sup>38</sup> Thus, OV can reasonably be considered as “grippers” that can effectively anchor nitrate ions to the metal–semiconductor catalyst. Based on the above description, the design and synthesis of metal–semiconductor electrocatalysts with OV are expected to promote the electro-reduction of nitrates to ammonium.

Herein,  $\text{Cu-Fe}_2\text{O}_3\text{-}x$  nanotubes with OV (labeled as  $\text{Cu-Fe}_2\text{O}_3\text{-}x$ ) were designed and prepared on three-dimensional Cu foams (CF) and adopted as efficient electrocatalysts for ENRA as these materials exhibit promising advantages with respect to cost, efficiency, stability, and scalability (Fig. S1, S2 and Tables S1, S2, ESI†). The built-in electric field generated by electron transfer at the interface between the metal and semiconductor, as well as the oxygen vacancies on the surface of the semiconductor, promoted ENRA. The OV in  $\text{Cu-Fe}_2\text{O}_3\text{-}60$  exhibited high adsorption energy for  $\text{NO}_3^-$  and high  $\text{H}_2$  generation energy, which inhibited the generation of  $\text{H}_2$ . This work verifies the effect of built-in electric field and OV in enhancing nitrate electroreduction both theoretically and experimentally and provides ideas for the development of low-cost, efficient and stable electrocatalysts for full-scale application to achieving energy efficiency, emission reduction and environmental protection.

## 2. Experimental section

### 2.1 Chemicals and materials

Sodium hydroxide ( $\text{NaOH}$ ,  $\geq 96.0\%$ ), ammonium persulphate ( $(\text{NH}_4)_2\text{S}_2\text{O}_8$ ,  $\geq 98.0\%$ ), iron nitrate nonahydrate ( $\text{Fe}(\text{NO}_3)_3 \cdot 9\text{H}_2\text{O}$ ,  $\geq 98.0\%$ ), ammonium sulfate- $^{14}\text{N}$  ( $(^{14}\text{NH}_4)_2\text{SO}_4$ , 98.5%), ammonium sulfate- $^{15}\text{N}$  ( $(^{15}\text{NH}_4)_2\text{SO}_4$ ,  $\geq 99$  at%, 98.5%), sodium nitrate- $^{14}\text{N}$  ( $\text{Na}^{14}\text{NO}_3$ , 98.5%), sodium nitrate- $^{15}\text{N}$  ( $\text{Na}^{15}\text{NO}_3$ ,  $^{15}\text{N} \geq 99$  at%, 98.5%), maleic acid ( $\text{C}_4\text{H}_4\text{O}_4$ ,  $\geq 99.0\%$ ), deuterium oxide ( $\text{D}_2\text{O}$ , 99 at% D) were bought from commercial sources. Milli-Q water ( $18.25 \text{ M}\Omega \text{ cm}^{-1}$ ) was used across all the experiments. Before use, Cu foam (CF, pore density 120 PPI) was ultrasonically rinsed in acetone, ethanol, and deionized water for 15 minutes to completely remove surface impurities and natural oxides.<sup>39</sup>

### 2.2 Synthesis of the $\text{Cu-Fe}_2\text{O}_3$ nanostructure

The  $\text{Cu-Fe}_2\text{O}_3$  nanostructure on CF was synthesized *via* three steps. Based on the method reported previously by our group,  $\text{Cu}(\text{OH})_2$  nanowires (NWs) were successfully grown on the

surface of CF by *in situ* oxidation.<sup>40</sup> The color of the Cu foams changed from orange–red to blue (see Fig. S3, ESI†). The as-prepared  $\text{Cu}(\text{OH})_2$  NWs were immersed in a 10 mM  $\text{Fe}^{3+}$  solution for some time, and a unique  $\text{Cu}(\text{OH})_2\text{-Fe}(\text{OH})_3$  nanostructure was obtained at room temperature. The color of the sample changed to brown–yellow after washing and drying. The prepared samples were denoted as  $\text{Cu}(\text{OH})_2\text{-Fe}(\text{OH})_3\text{-}x$  ( $x$  is the immersion time). Then, a heat treatment was carried out under the air for 2 h at 300 °C at a heating rate of 2 °C  $\text{min}^{-1}$ , after which  $\text{CuO-Fe}_2\text{O}_3\text{-}x$  was obtained. The color changed from brown–yellow to dark-red during this step. The  $\text{Cu-Fe}_2\text{O}_3\text{-}x$  with OV were obtained by chronopotentiometric electroreduction performed at the current density of 20  $\text{mA cm}^{-1}$ . The color of  $\text{Cu-Fe}_2\text{O}_3\text{-}x$  was black (see Fig. S3, ESI†). The details of the samples are listed in Table S3 (ESI†).

## 3. Results and discussion

### 3.1 Materials characterization

The  $\text{Cu-Fe}_2\text{O}_3\text{-}x$  NTs were prepared by a three-step process (For details, see Fig. 1a and the Experimental section). First, uniform  $\text{Cu}(\text{OH})_2$  nanowire arrays were directly grown on the skeleton of the copper foam by a surface oxidation process. The foam was then immersed into a 10 mM  $\text{Fe}^{3+}$  solution to obtain a unique  $\text{Cu}(\text{OH})_2\text{-Fe}(\text{OH})_3\text{-}x$  ( $x$  is the immersion time) (Fig. S4, ESI†). Interestingly, the wall thickness of the nanotubes could be regulated by controlling the immersion time (Fig. S4, ESI†). After air heating and electroreduction,  $\text{Cu-Fe}_2\text{O}_3\text{-}x$  (with an average length and mass loading of  $\approx 1.3 \mu\text{m}$  and  $0.89 \text{ mg cm}^{-2}$ , respectively) were successively obtained (Fig. 1b and Fig. S5, ESI†). At the same time, by comparing the scanning electron microscopic (SEM) images of  $\text{Cu-Fe}_2\text{O}_3\text{-}30$ , 60, and 120, we found that when the immersion time was increased to 120s, the nanotube structure broke and was unfavorable for the catalytic reaction. Therefore, we chose  $\text{Cu-Fe}_2\text{O}_3\text{-}60$  as the experimental material for specific research. As shown in Fig. 1c, the transmission electron microscopic (TEM) images of  $\text{Cu-Fe}_2\text{O}_3\text{-}60$  at different magnifications showed that the inner diameter of the nanotubes, which were composed of nanoparticles, remained at about 190 nm. In addition, the hybridization distribution of the elements in  $\text{Cu-Fe}_2\text{O}_3\text{-}60$  was further confirmed by the corresponding crossing-sectional composition line profiles. As shown in Fig. 1d, in  $\text{Cu-Fe}_2\text{O}_3\text{-}60$ , Cu, Fe, and O were evenly distributed in the measured area, which proves that molecular thermal diffusion promoted the hybrid distribution of elements. The elemental hybrid distribution in  $\text{Cu-Fe}_2\text{O}_3\text{-}60$  was additionally confirmed by the element mappings (Fig. 1e–h). As shown in Fig. 1i, the HR-TEM image of  $\text{Cu-Fe}_2\text{O}_3\text{-}60$  clearly showed the 0.208, 0.295, and 0.252 nm lattice spacings corresponding to the plane of  $\text{Cu}(111)$ ,  $\text{Fe}_2\text{O}_3(220)$ ,  $\text{Fe}_2\text{O}_3(311)$ , respectively.<sup>41,42</sup> The crystalline phase of the as-prepared sample was characterized using the XRD patterns (Fig. 1j). Except for the diffraction peaks assigned to the Cu (JCPDS No. 04-0836) phase,<sup>43</sup> the other diffraction peaks were consistent with those of the standard  $\text{Fe}_2\text{O}_3$  (JCPDS No. 21-0920) (JCPDS



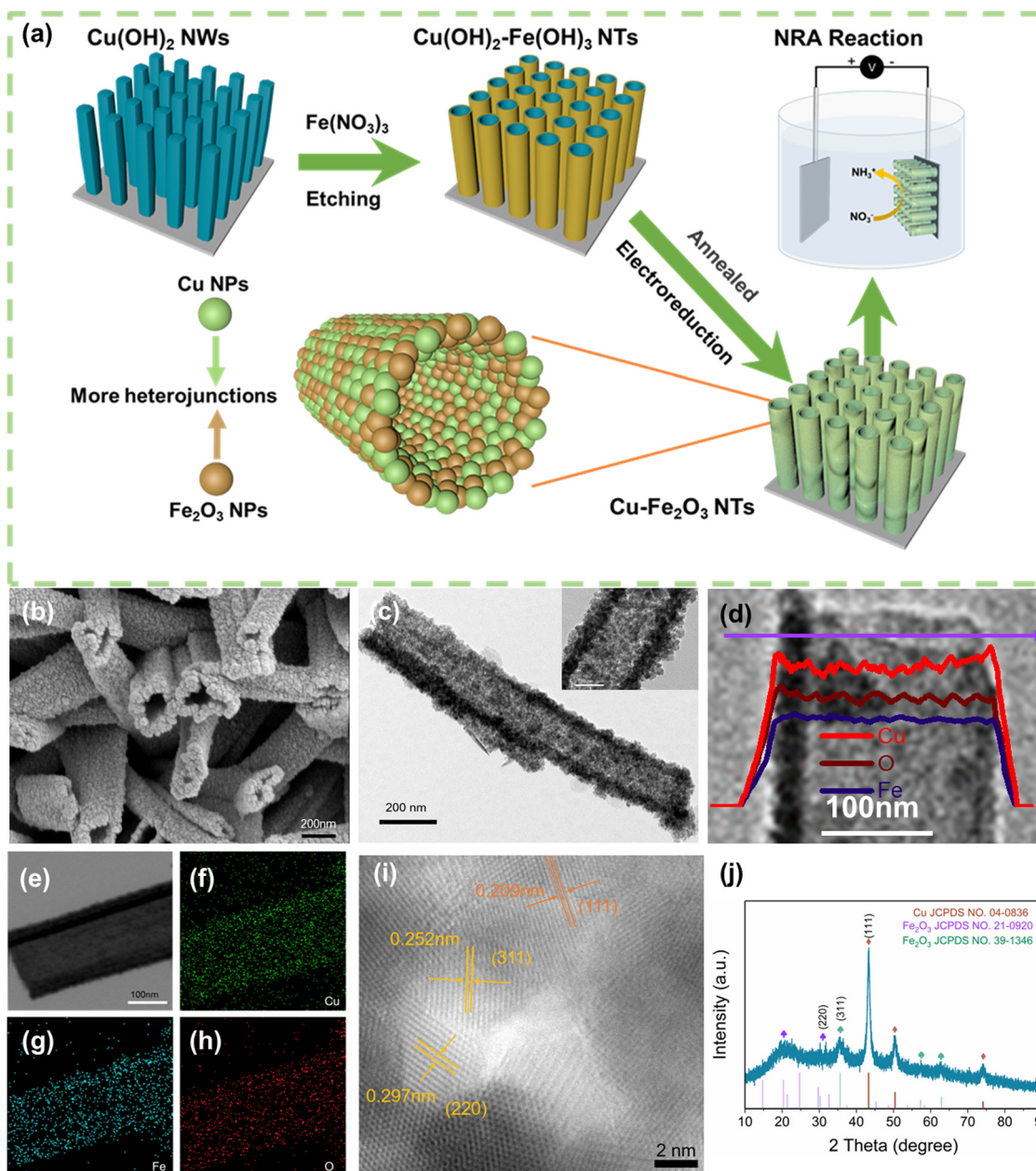


Fig. 1 (a) Schematic of defective Cu-Fe<sub>2</sub>O<sub>3</sub> synthesis. (b) The SEM image (c) TEM image, (d) elemental concentration profile images, (e–h) elemental mapping images, (i) HR-TEM image, (j) XRD pattern of Cu-Fe<sub>2</sub>O<sub>3</sub>-60.

No. 39-1346) phase.<sup>44</sup> The above results show that Cu-Fe<sub>2</sub>O<sub>3</sub>-60 nanotubes composed of nano-Cu and nano-Fe<sub>2</sub>O<sub>3</sub> were successfully synthesized by the proposed method.

As an electrocatalyst, its surface chemical composition and interface properties would directly affect its catalytic performance; therefore, these characteristics were further analyzed by XPS and EPR. As shown in Fig. 2a and b, charge transfer at the interface of Cu-Fe<sub>2</sub>O<sub>3</sub>-60 was investigated. First, the typical Cu, Fe 2p XPS spectra of CuO-Fe<sub>2</sub>O<sub>3</sub> and Cu-Fe<sub>2</sub>O<sub>3</sub>-60 were obtained to further clarify the electron redistribution.<sup>30</sup> Compared with CuO-Fe<sub>2</sub>O<sub>3</sub>, Cu-Fe<sub>2</sub>O<sub>3</sub>-60 had additional main peaks at 932.8 eV and 952.8 eV, which were attributed as the characteristic peaks of Cu 2p<sub>3/2</sub> and Cu 2p<sub>1/2</sub> of Cu<sup>0</sup>, respectively

(Fig. 2a).<sup>45</sup> Compared with Cu (932.4 eV and 952.2 eV for Cu<sup>0</sup>),<sup>46</sup> the binding energy of Cu<sup>0</sup> in Cu-Fe<sub>2</sub>O<sub>3</sub>-60 appeared to have shifted slightly in the positive direction, indicating the decreased electron density of metal Cu in Cu-Fe<sub>2</sub>O<sub>3</sub>-60 due to electron loss.<sup>47</sup> Simultaneously, the slight negative shifts (*ca.* 0.3 eV for Fe 2p<sub>3/2</sub> and 0.4 eV for Fe 2p<sub>1/2</sub>) in the binding energy of Fe<sup>3+</sup> in Cu-Fe<sub>2</sub>O<sub>3</sub>-60 compared with CuO-Fe<sub>2</sub>O<sub>3</sub> (710.7 and 724.3 eV) suggested that Cu-Fe<sub>2</sub>O<sub>3</sub>-60 had gained electrons and become an electron-rich body on the Fe<sub>2</sub>O<sub>3</sub> side (Fig. 2b).<sup>48,49</sup> The O 1s XPS and EPR were examined to confirm the presence of more OV<sub>s</sub> in Cu-Fe<sub>2</sub>O<sub>3</sub>-*x*. The O 1s XPS spectra (Fig. 2c) showed three peaks centered at 530.2, 531.4 and 532.6 eV, corresponding to lattice oxygen (O<sub>L</sub>), oxygen vacancies (O<sub>V</sub>) and



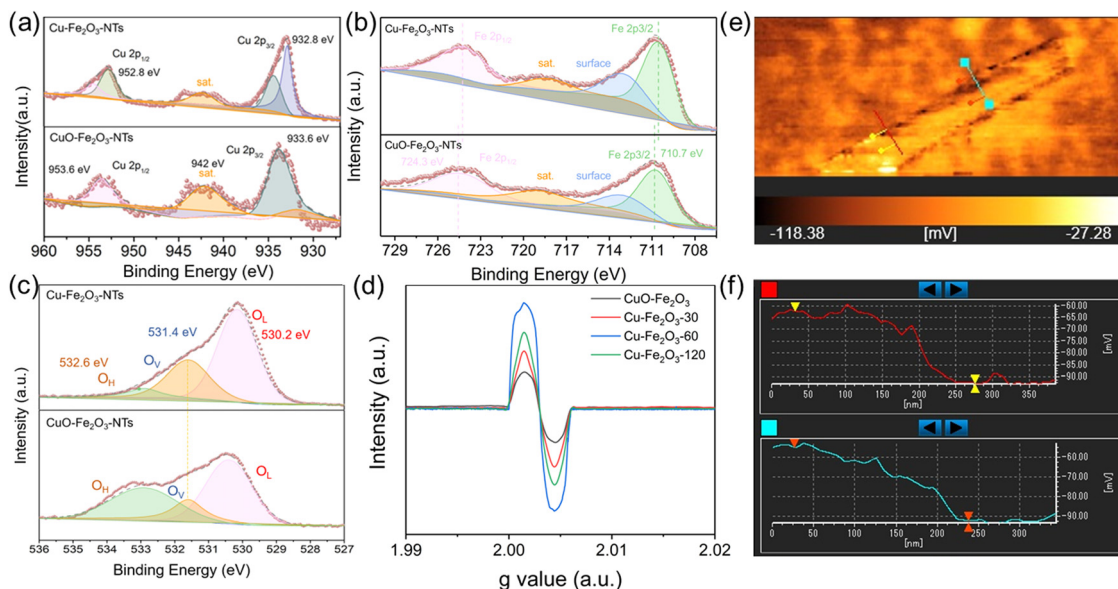


Fig. 2 High-resolution XPS spectra of Cu-Fe<sub>2</sub>O<sub>3</sub>-60 and CuO-Fe<sub>2</sub>O<sub>3</sub>. (a) The Cu 2p, (b) Fe 2p, and (c) O 1s spectra. (d) The EPR spectra of Cu-Fe<sub>2</sub>O<sub>3</sub>-x and CuO-Fe<sub>2</sub>O<sub>3</sub>. (e) The built-in electric field distribution of Cu-Fe<sub>2</sub>O<sub>3</sub>-60. (f) Surface potential values extracted across the lines in e.

hydroxyl groups (O<sub>H</sub>), respectively.<sup>50</sup> The area ratios of the O<sub>V</sub> peak relative to the total area of the O<sub>L</sub>, O<sub>V</sub> and O<sub>H</sub> peaks [ $SO_V / (SO_L + SO_V + SO_H)$ ] were 11.12% and 34.99% for CuO-Fe<sub>2</sub>O<sub>3</sub> and Cu-Fe<sub>2</sub>O<sub>3</sub>-60, respectively. The larger area percentage at ~531.4 eV in the Cu-Fe<sub>2</sub>O<sub>3</sub>-60 spectrum indicates that the concentration of OV<sub>s</sub> in Cu-Fe<sub>2</sub>O<sub>3</sub>-60 was much higher than that in CuO-Fe<sub>2</sub>O<sub>3</sub> due to the electroreduction treatment. Besides, compared with Cu-Fe<sub>2</sub>O<sub>3</sub>-30 and Cu-Fe<sub>2</sub>O<sub>3</sub>-120 after electroreduction, Cu-Fe<sub>2</sub>O<sub>3</sub>-60 exhibited a stronger EPR signal

at  $g = 2.003$ , indicating that a higher concentration of OV<sub>s</sub> in Cu-Fe<sub>2</sub>O<sub>3</sub>-60 (Fig. 2d).<sup>51</sup> The above results prove that electron transfer from metallic Cu to semiconductor Fe<sub>2</sub>O<sub>3</sub> at the interface of Cu-Fe<sub>2</sub>O<sub>3</sub>-60 and the electroreduction treatment could create much more OV<sub>s</sub> in Cu-Fe<sub>2</sub>O<sub>3</sub>-x.<sup>52</sup> The change in the built-in electric field in Cu-Fe<sub>2</sub>O<sub>3</sub>-x due to electron transfer was further studied. As shown in Fig. 2e and Fig. S6, (ESI<sup>†</sup>) we used a Kelvin probe atomic force microscope to analyze the surface charge of Cu-Fe<sub>2</sub>O<sub>3</sub>-x. Compared with Cu-Fe<sub>2</sub>O<sub>3</sub>-30 (12.76 mV)

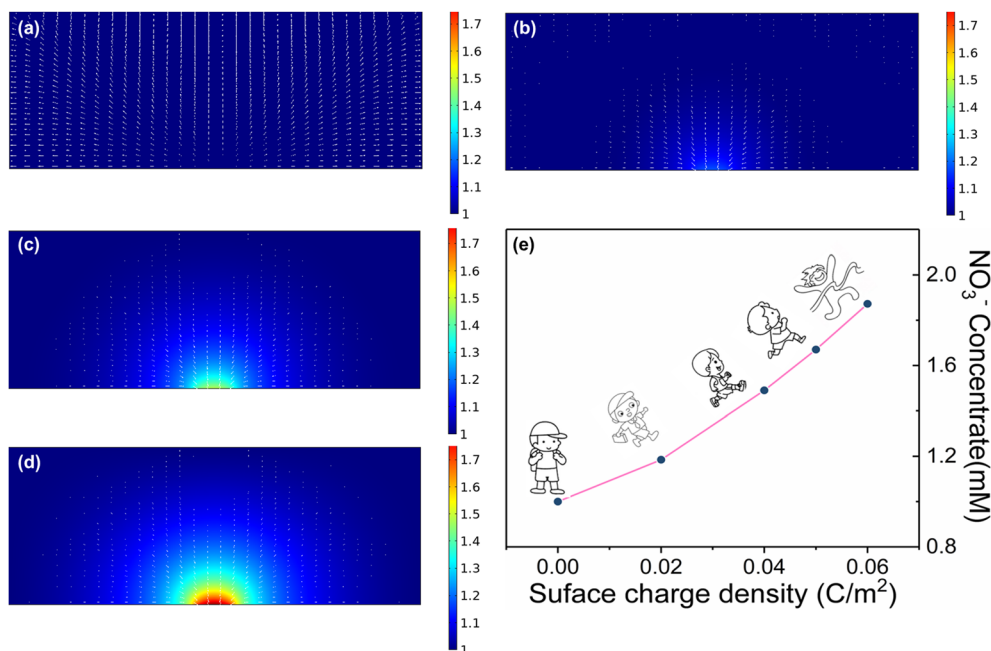


Fig. 3 Nitrate distribution on the electrode after introducing a small number of charges: (a) 0 C m<sup>-2</sup>, (b) 0.02 C m<sup>-2</sup>, (c) 0.04 C m<sup>-2</sup>, (d) 0.06 C m<sup>-2</sup>. (e) The line graph of surface charge density and surface-enriched nitrate anion density.



and Cu-Fe<sub>2</sub>O<sub>3</sub>-120 (19.96 mV), the contact potential difference between the internal Cu and Fe<sub>2</sub>O<sub>3</sub> heterogeneous interface and Si substrate in Cu-Fe<sub>2</sub>O<sub>3</sub>-60 (32.62 mV) was more negative (Fig. 2f). In other words, it is logical to believe that the negatively charged surface field on Fe<sub>2</sub>O<sub>3</sub> NPs expands by accepting more electrons from Cu NP-based electron donors in Cu-Fe<sub>2</sub>O<sub>3</sub>-60.

We directly associate the built-in electric field with the enrichment of nitrate ions near the catalyst. To understand the catalytic enhancement effect of the built-in electric field, we further simulated the nitrate enrichment process using finite element analysis. As shown in Fig. 3a-d and Fig. S7 (ESI<sup>†</sup>), to quantitatively calculate the influence of the electric field on the concentration of nitrate on the surface, we used a two-dimensional plane model to simulate the enrichment of nitrate ion density near the electrode. Compared with the negligible neutral surface, the charged electrode with a local electric field could greatly increase the nitrate ion density, and the stronger the electric field was, the more obvious the nitrate enrichment effect. More importantly, the nitrate anion density on the simulated heterogeneous interface increased from 1 to 1.87 mM with the introduction of a small number of charges (0.06 C m<sup>-2</sup>), theoretically demonstrating the key role of the built-in electric field in enhancing the enrichment of nitrate anions (Fig. 3e).

### 3.2 Electrochemical nitrate reduction activity

The ENRA performance of Cu-Fe<sub>2</sub>O<sub>3</sub>-*x* was evaluated by using a typical three-electrode system (Fig. S8, ESI<sup>†</sup>). The concentrations of nitrate, nitrite, and ammonium in the electrolyte before and after the test were determined by colorimetric methods (Fig. S9, ESI<sup>†</sup>).<sup>53-55</sup> Before the experiment, we measured the electrochemical double-layer capacitance by cyclic voltammetry and then compared the electrochemical surface area (ECSA) of the different catalysts. As shown in Fig. S10 and Table S4 (ESI<sup>†</sup>),

the ECSAs of Cu-Fe<sub>2</sub>O<sub>3</sub>-30, Cu-Fe<sub>2</sub>O<sub>3</sub>-60 and Cu-Fe<sub>2</sub>O<sub>3</sub>-120 were 27.51, 40.53 and 33.91 cm<sup>2</sup>, respectively, which preliminarily reflect the catalytic superiority of Cu-Fe<sub>2</sub>O<sub>3</sub>-60. Then, LSV measurements of Cu-Fe<sub>2</sub>O<sub>3</sub>-30, 60, and 120 were performed in a 0.5 M Na<sub>2</sub>SO<sub>4</sub> solution with and without 50 ppm NO<sub>3</sub><sup>-</sup>-N (Fig. 4a and Fig. S11, ESI<sup>†</sup>). The current density increased significantly at -0.3 V vs. RHE with the addition of NO<sub>3</sub><sup>-</sup>, suggesting that NO<sub>3</sub><sup>-</sup> in the solution participated in the reduction reactions. Thus, the nitrate reduction reactions on Cu-Fe<sub>2</sub>O<sub>3</sub>-30, 60 and 120 were studied in the potential range from -0.3 to -0.7 V vs. RHE (Fig. S12, ESI<sup>†</sup>). Under the same potential, the nitrate conversion rate, ammonium selectivity and yield rate of Cu-Fe<sub>2</sub>O<sub>3</sub>-60 were obviously higher than those of Cu-Fe<sub>2</sub>O<sub>3</sub>-30 and Cu-Fe<sub>2</sub>O<sub>3</sub>-120. Based on the above results, Cu-Fe<sub>2</sub>O<sub>3</sub>-60 was selected for follow-up research. From -0.3 V to -0.7 V vs. RHE, the conversion rate of NO<sub>3</sub><sup>-</sup> increased gradually, while the Faraday efficiency showed a volcano-shaped curve, which reached a maximum of 80.1% at -0.6 V vs. RHE (Fig. 4b). In addition, Fig. 4c displays the selectivity and yield of ammonium at different potentials. The results show that the optimal selectivity of 88.47% and the yield rate of 0.108 mmol h<sup>-1</sup> cm<sup>-2</sup> were achieved at -0.6 V vs. RHE. Meanwhile, the selectivity of NO<sub>2</sub><sup>-</sup>-N and NH<sub>4</sub><sup>+</sup>-N both tended to reach the optimal value at -0.6 V vs. RHE (Fig. S13, ESI<sup>†</sup>). Therefore, we chose -0.6 V vs. RHE as the operational potential for the ENRA activity test. With the prolongation of the reduction reaction time, the concentration of NO<sub>3</sub><sup>-</sup>-N continuously decreased, while the concentration of NH<sub>4</sub><sup>+</sup>-N increased, which means that NO<sub>3</sub><sup>-</sup>-N was reduced to NH<sub>4</sub><sup>+</sup>-N. At the same time, the concentration of NO<sub>2</sub><sup>-</sup>-N ramped up first and then declined, indicating that the reaction had high selectivity for ammonium (Fig. 4d). Simultaneously, the nitrite selectivity of Cu-Fe<sub>2</sub>O<sub>3</sub>-30, Cu-Fe<sub>2</sub>O<sub>3</sub>-60, Cu-Fe<sub>2</sub>O<sub>3</sub>-120 decreased gradually and tended to a lower value at -0.6 V vs. RHE, which further

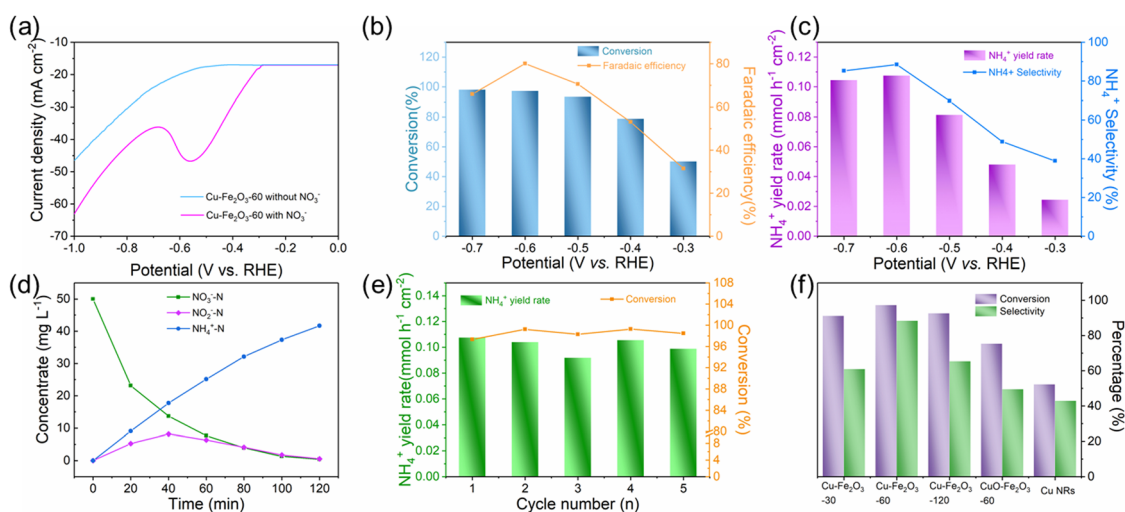


**Fig. 4** (a) The LSV curves of Cu-Fe<sub>2</sub>O<sub>3</sub>-60 in 0.5 M Na<sub>2</sub>SO<sub>4</sub> with and without 50 ppm NO<sub>3</sub><sup>-</sup>-N. (b) The faradaic efficiency of ammonium and the conversion rate of nitrate over Cu-Fe<sub>2</sub>O<sub>3</sub>-60. (c) The selectivity and yield rate of ammonium over Cu-Fe<sub>2</sub>O<sub>3</sub>-60. (d) Concentrate-time curves of nitrate, nitrite, and ammonium over Cu-Fe<sub>2</sub>O<sub>3</sub>-60 at -0.6 V vs. RHE. (e) The conversion of nitrate and yield rate of ammonium after consecutive recycling test at -0.6 V vs. RHE. (f) The conversion rates of nitrate and selectivity for ammonium over different samples at -0.6 V vs. RHE.



proved the high selectivity for the reduction of nitrate to ammonium (Fig. S14, ESI<sup>†</sup>). Moreover, the nitrate conversion and ammonium yield rate of Cu-Fe<sub>2</sub>O<sub>3</sub>-60 showed no obvious decay after five consecutive recycling tests using the same piece of catalyst, confirming its excellent stability (Fig. 4e). In addition, Cu-Fe<sub>2</sub>O<sub>3</sub>-60 still retained the original tubular array morphology (Fig. S15, ESI<sup>†</sup>). At the same time, the XRD and XPS data of the tested samples also showed that the phase of Cu-Fe<sub>2</sub>O<sub>3</sub>-60 had not changed significantly (Fig. S16, ESI<sup>†</sup>). Finally, the performance of Cu-Fe<sub>2</sub>O<sub>3</sub>-30, Cu-Fe<sub>2</sub>O<sub>3</sub>-120, CuO-Fe<sub>2</sub>O<sub>3</sub>-60 and Cu NWs was studied and compared with that of Cu-Fe<sub>2</sub>O<sub>3</sub>-60. As shown in Fig. 4f, the conversion rate of NO<sub>3</sub><sup>-</sup> and selectivity for ammonium were 91.25% and 60.96% over Cu-Fe<sub>2</sub>O<sub>3</sub>-30, 92.72% and 65.43% over Cu-Fe<sub>2</sub>O<sub>3</sub>-120, 75.46% and 49.59% over CuO-Fe<sub>2</sub>O<sub>3</sub>-60, and 52.35% and 42.96% over Cu NWs, respectively, which were significantly lower than those of Cu-Fe<sub>2</sub>O<sub>3</sub>-60 (conversion rate of NO<sub>3</sub><sup>-</sup>: 97.33%, selectivity of ammonium: 88.47%). Compared with Cu-Fe<sub>2</sub>O<sub>3</sub>-60, the yield of ammonium while using Cu-Fe<sub>2</sub>O<sub>3</sub>-30, Cu-Fe<sub>2</sub>O<sub>3</sub>-120, CuO-Fe<sub>2</sub>O<sub>3</sub>-60 and Cu NWs at -0.6 V vs. RHE was also far from satisfactory (Fig. S17, ESI<sup>†</sup>). Based on the previous evaluation of the built-in electric field and oxygen vacancies in Cu-Fe<sub>2</sub>O<sub>3</sub>-x, we could conclude that the best catalytic performance of Cu-Fe<sub>2</sub>O<sub>3</sub>-60 was due to the positive effect of the built-in electric field and oxygen vacancies. To expand this experiment from the laboratory to industrial scale, we constructed a 180 L pilot-scale reactor that used Cu-Fe<sub>2</sub>O<sub>3</sub>-60 integrated with a titanium plate to convert nitrate to ammonium in simulated wastewater. Fig. S18 (ESI<sup>†</sup>) shows the physical setup of the reactor, in which the internal circulation was implemented by using a circulating pump to enhance mass transfer to amplify the overall performance of electrocatalysis. As shown in Fig. 5, the concentrate-time curves of nitrate and ammonium were recorded under different current densities. It was found that a conversion rate close to 85% was maintained at the current density of 20 mA cm<sup>-2</sup>, which preliminarily supports the application of the catalyst at

the industrial scale. The above results show that Cu-Fe<sub>2</sub>O<sub>3</sub>-60, which exhibits high catalytic activity, selectivity and stability in both experimental and industrial settings, is suitable for large-scale application in ENRA.

To eliminate possible interferences from the electrocatalyst itself or the environment, the electrochemical measurement was performed in the pure Na<sub>2</sub>SO<sub>4</sub> electrolyte (Fig. 6a), and the result showed that the generation of ammonium could be ignored. In addition, <sup>15</sup>N isotope labeling experiments were implemented to verify the sources of ammonium, and the yield rate of ammonium was quantified by the <sup>1</sup>H NMR spectra.<sup>56-59</sup> We carried out electrochemical measurements at -0.6 V vs. RHE for 2.0 h in the solutions with Na<sup>15</sup>NO<sub>3</sub> and Na<sup>14</sup>NO<sub>3</sub> as the N sources, respectively. As shown in Fig. 6b, when the electrocatalytic reduction was implemented in the solution with Na<sup>15</sup>NO<sub>3</sub>, the <sup>1</sup>H NMR spectra of the products showed the representative double peaks of <sup>15</sup>NH<sub>4</sub><sup>+</sup> at δ = 6.97 and 7.09 ppm, and there was no triple peak representing <sup>14</sup>NH<sub>4</sub><sup>+</sup> at δ = 6.94, 7.03 and 7.12 ppm (Fig. 6b). This result proves that the ammonium produced by electrocatalytic reduction came entirely from nitrate. Maleic acid (C<sub>4</sub>H<sub>4</sub>O<sub>4</sub>) was used as the external standard for quantifying the produced <sup>15</sup>NH<sub>4</sub><sup>+</sup>-N and <sup>14</sup>NH<sub>4</sub><sup>+</sup>-N products (Fig. S19 and S20, ESI<sup>†</sup>). The standard curve of the integral area against the concentration of NH<sub>4</sub><sup>+</sup>-N was established to determine the concentration of <sup>15</sup>NH<sub>4</sub><sup>+</sup>-N or <sup>14</sup>NH<sub>4</sub><sup>+</sup>-N (Fig. 6c and d). The quantitative <sup>1</sup>H NMR results of ammonium produced were very close to the quantitative results from the colorimetric methods (Table S5, ESI<sup>†</sup>), which confirms the accuracy of the different quantitative methods.

Based on the excellent catalytic performance of Cu-Fe<sub>2</sub>O<sub>3</sub>-60, the enhancement mechanism of OV and the reaction path of nitrate electroreduction in Cu-Fe<sub>2</sub>O<sub>3</sub>-60 were explored by the *in situ* Raman test and theoretical calculations. For comparison, the Fe<sub>2</sub>O<sub>3</sub>(220) surface without OVs and with OVs were

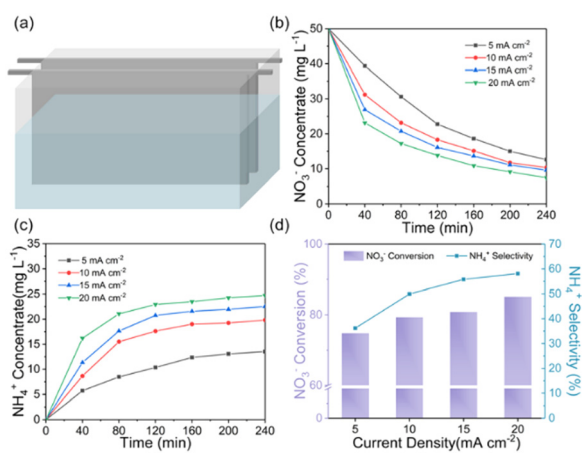


Fig. 5 (a) Schematic of the pilot-scale electrochemical reactor. The concentrate-time curves of (a) nitrate and (b) ammonium over Cu-Fe<sub>2</sub>O<sub>3</sub>-60. (c) The nitrate conversion rate and ammonium selectivity of Cu-Fe<sub>2</sub>O<sub>3</sub>-60 under different current densities.

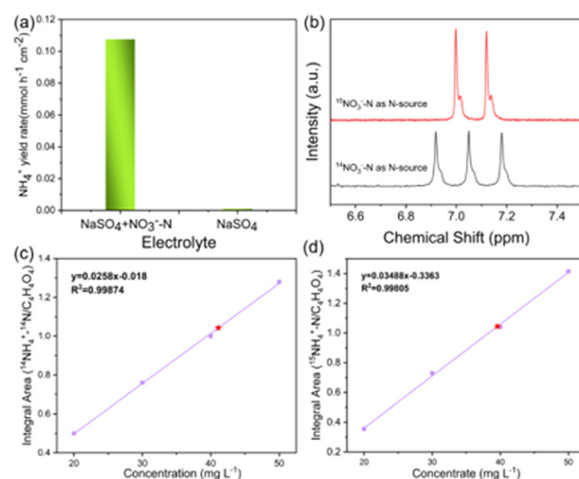


Fig. 6 (a) The ammonia yield over Cu-Fe<sub>2</sub>O<sub>3</sub>-60 in the 0.5 M Na<sub>2</sub>SO<sub>4</sub> electrolyte with and without NO<sub>3</sub><sup>-</sup>. (b) <sup>1</sup>H NMR spectra of the electrolyte while using <sup>15</sup>NO<sub>3</sub><sup>-</sup>-N and <sup>14</sup>NO<sub>3</sub><sup>-</sup>-N as the nitrogen sources. The standard curves of (c) the integral area of (<sup>14</sup>NH<sub>4</sub><sup>+</sup>-N/C<sub>4</sub>H<sub>4</sub>O<sub>4</sub>) against <sup>14</sup>NH<sub>4</sub><sup>+</sup>-N concentration, and (d) the integral area of (<sup>15</sup>NH<sub>4</sub><sup>+</sup>-N/C<sub>4</sub>H<sub>4</sub>O<sub>4</sub>) against <sup>15</sup>NH<sub>4</sub><sup>+</sup>-N concentration.



chosen as models (Fig. S21, ESI<sup>†</sup>). The adsorption energy of  $\text{NO}_3^-$  on  $\text{Fe}_2\text{O}_3(220)$  with OV was  $-2.38$  eV, which was much higher than that on  $\text{Fe}_2\text{O}_3(220)$  without OV ( $-1.02$  eV) (Fig. 7a). This result confirmed the key role of OV in anchoring  $\text{NO}_3^-$ . In other words, the existence of OV promoted the initial anchoring of  $\text{NO}_3^-$  on the catalyst surface, and the strong anchoring of  $\text{NO}_3^-$  on the catalyst surface will inhibit the competitive anchoring of other anions in the solution, thus ensuring the overall reduction reaction process. Hence, the anchoring mechanism of OV should be considered an important factor that favors the subsequent reduction reaction of  $\text{NO}_3^-$  along with the proton-electron pairs. Additionally, the energy barrier of  $\text{H}_2$  formation on  $\text{Cu-Fe}_2\text{O}_3$ -60 with OV was  $1.6$  eV, which was higher than that on  $\text{Cu NWs}$  ( $1.27$  eV), indicating poor HER activity over the  $\text{Cu-Fe}_2\text{O}_3$  NTs (Fig. 7b). Then, the *in situ* Raman spectra were recorded to capture the adsorbed intermediates on the electrode.<sup>60</sup> Fig. 7c displays the absorbance spectra from  $-0.3$  to  $-0.8$  V vs. RHE. During electrocatalytic nitrate reduction, an obvious Raman characteristic peak was observed at  $1045$   $\text{cm}^{-1}$ , which was attributed to the stretching vibration of adsorbed  $\text{NO}_3^-$ .<sup>61</sup> Surprisingly, a significant Raman peak was observed at  $1315$ – $1330$   $\text{cm}^{-1}$ , which could be designated to ammonia adsorption.<sup>62</sup> In addition, the characteristic peak observed at  $1375$   $\text{cm}^{-1}$  could be assigned to the antisymmetric stretching of  $\text{NO}_2^-$  in nitrate during the electrocatalytic nitrate reduction process.<sup>61</sup> Theoretically, the Raman shift of  $\text{NH}_4^+$  is around  $1400$   $\text{cm}^{-1}$  and  $1480$   $\text{cm}^{-1}$ ,<sup>63</sup> but its Raman signal could not be detected due to its weak intensity in water. However, colorimetric methods and nuclear magnetic resonance have long been used to prove the existence of  $\text{NH}_4^+$ . The schematic of

the built-in electric field formation and electrocatalytic reduction is shown in Fig. 7d. When metals and semiconductors are placed together, spontaneous charge directional movement occurs at their interface, thereby resulting in a built-in electric field. As the external driving force of nitrate enrichment, the built-in electric field plays a vital role. Based on the spontaneous electron transfer from  $\text{Cu}$  to  $\text{Fe}_2\text{O}_3$ , the built-in electric field verified by KPFM promotes the enrichment of  $\text{NO}_3^-$  at the interface, which solves the problem of slow mass transfer of nitrate in the solution. The OV acts as grippers and anchor the  $\text{NO}_3^-$  at the interface, giving rise to the adsorbed nitrate state ( $\text{NO}_3^*$ ), which completes the overall reduction reaction due to the action of proton-electron pairs. Based on the above intermediates detected in the *in situ* Raman spectra and reported in the literature,<sup>64</sup> we propose the steps of the whole process from the anchoring of OV to the recovery of OV after the reduction of nitrate to ammonium (Fig. 7e). The three O atoms in  $\text{NO}_3^-$  are labeled as O1, O2 and O3, respectively. For  $\text{NO}_3^-$  anchoring on the  $\text{Cu-Fe}_2\text{O}_3$ -60 surface with vacancies, O1 of  $\text{NO}_3^-$  fills in the OV site to form  $\text{NO}_3^*$ . The N-O3 bond is broken by the action of the proton-electron pairs to form  $\text{NO}_2^*$  and  $\text{H}_2\text{O}$ . Then, by adsorbing a proton to couple with an electron transfer, the N-O2 bond in  $\text{NO}_2^*$  is broken, and  $\text{NO}_2^*$  is converted to  $\text{H}_2\text{NO}^*$ . Subsequently,  $\text{H}_2\text{NO}^*$  couples with the proton-electron pairs to form  $\text{NH}_4^+$ , leaving O1 on the OV site. Finally, the O filling the OV site is reduced to  $\text{H}_2\text{O}$  by protons to restore the oxygen vacancy on the surface. Based on the built-in electric field and OV of  $\text{Cu-Fe}_2\text{O}_3$ -60, an assembly-line electrocatalytic reduction route for the recovery of the nitrate-anchoring vacancies, thereby achieving a cycle-efficient catalytic effect.

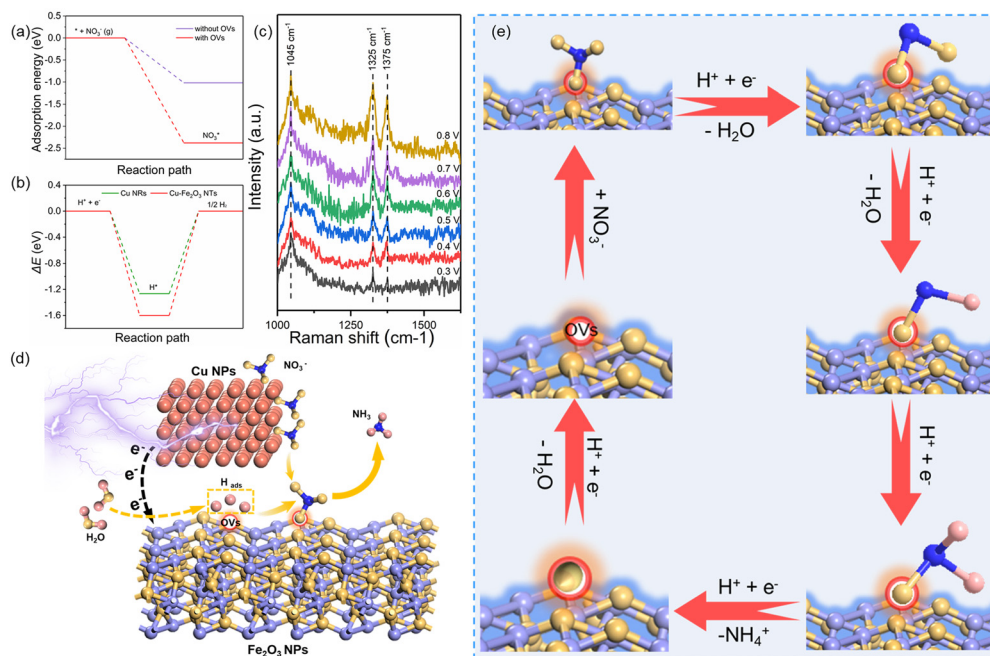


Fig. 7 (a) The calculated adsorption energies of  $\text{NO}_3^-$  on the  $\text{Fe}_2\text{O}_3(220)$  surfaces with and without OV. (b) The calculated relative reaction energy of  $\text{H}_2$  formation on  $\text{Cu NWs}$  and  $\text{Cu-Fe}_2\text{O}_3$ -60. (c) The *in situ* Raman spectra of  $\text{Cu-Fe}_2\text{O}_3$ -60. (d) The mechanism diagram. (e) The electrocatalytic reduction path diagram.



## 4. Conclusions

In summary, we successfully synthesized Cu-Fe<sub>2</sub>O<sub>3</sub>-60, which exhibits excellent catalytic activity, faradaic efficiency, and selectivity for nitrate electroreduction. The XPS, KPFM and EPR results confirmed the formation of a built-in electric field and OV. Based on the enhancement effect of the built-in electric field and OVs, we have reasonably proposed an assembly-line electroreduction route for nitrate enrichment *via* anchoring. Under the optimal potential, the nitrate conversion rate, faradaic efficiency and selectivity for ammonium reached 97.33%, 80.1%, and 88.47%, respectively. The <sup>15</sup>N isotope labeling experiment certified that ammonium was produced solely from nitrate electroreduction. The accuracy of the data was verified mutually by <sup>1</sup>H NMR spectroscopy and colorimetric methods. Based on the results of *in situ* Raman spectroscopy and the colorimetric methods, we deduced the reaction path. The results of the theoretical calculations and structural model show that an oxygen atom in nitrate fills the OV site, which weakens N–O bonding and promotes the speed-controlling step of nitrate conversion. The subsequent intermediate generates the target ammonium and restores the oxygen vacancies on the surface under the action of proton–electron pairs. The assembly-line-like design for material engineering is conducive to solving the problem of low ammonium generation rate at low concentrations.

## Author contributions

Yihong Gao: conceptualization, investigation, formal analysis, data curation, methodology, writing – original draft, writing – review & editing; Kun Huang: conceptualization, investigation, formal analysis, data curation, validation; Chen Yan: theoretical calculation; Hui Zhang: methodology, investigation; Shikuo Li: methodology, investigation; Longjiu Cheng: formal analysis, performed the theoretical calculations; Fangzhi Huang: conceptualization, data curation, formal analysis, funding acquisition, resources, supervision.

## Conflicts of interest

There are no conflicts to declare.

## Acknowledgements

This work was supported by the National Natural Science Foundation of China (52172174 and 21771001), Key projects of quality engineering teaching and research in Anhui Province (2018jyxm0365), Anhui provincial key research and development plan (202004a07020026), the Program of Anhui Scientific and Technical Leaders Reserve Candidates (2018H168), the Scholar Program for the Outstanding Innovative Talent of College Discipline (Specialty), and open fund for Discipline Construction, Institute of Physical Science and Information Technology, Anhui University. Key Lab of Photovoltaic and

Energy Conservation Materials, Chinese Academy of Sciences is gratefully acknowledged by the authors.

## References

- N. Lehnert, H. T. Dong, J. B. Harland, A. P. Hunt and C. J. White, *Nat. Rev. Chem.*, 2018, **2**, 278–289.
- M. Duca and M. T. M. Koper, *Energy Environ. Sci.*, 2012, **5**, 9726–9742.
- Z. Zhang, Y. Xu, W. Shi, W. Wang, R. Zhang, X. Bao, B. Zhang, L. Li and F. Cui, *Chem. Eng. J.*, 2016, **290**, 201–208.
- K. N. Heck, S. Garcia-Segura, P. Westerhoff and M. S. Wong, *Acc. Chem. Res.*, 2019, **52**, 906–915.
- H. Niu, Z. Zhang, X. Wang, X. Wan, C. Shao and Y. Guo, *Adv. Funct. Mater.*, 2020, **31**, 2008533.
- E. Pérez Gallent, M. C. Figueiredo, I. Katsounaros and M. T. M. Koper, *Electrochim. Acta*, 2017, **227**, 77–84.
- W. Li, S. Patton, J. M. Gleason, S. P. Mezyk, K. P. Ishida and H. Liu, *Environ. Sci. Technol.*, 2018, **52**, 6417–6425.
- M. Alikhani and M. R. Moghbeli, *Chem. Eng. J.*, 2014, **239**, 93–104.
- K. M. Chon, Y. H. Lee, J. Traber and U. V. Gunten, *Water Res.*, 2013, **47**, 5381–5391.
- A. C. Alba-Rubio, J. L. G. Fierro, L. León-Reina, R. Mariscal, J. A. Dumesic and M. López Granados, *Appl. Catal., B*, 2017, **202**, 269–280.
- J. Ma, Q. Yang, S. Wang, L. Wang, A. Takigawa and Y. Peng, *J. Hazard. Mater.*, 2010, **175**, 518–523.
- S. J. Tesh and T. B. Scott, *Adv. Mater.*, 2014, **26**, 6056–6068.
- M. Markiewicz, J. Kumirska, I. Lynch, M. Matzke, J. Köser, S. Bemowsky, D. Docter, R. Stauber, D. Westmeier and S. Stolte, *Green Chem.*, 2018, **20**, 4133–4168.
- L. Su, D. Han, G. Zhu, H. Xu, W. Luo, L. Wang, W. Jiang, A. Dong and J. Yang, *Nano Lett.*, 2019, **19**, 5423–5430.
- W. Hong, L. Su, J. Wang, M. Jiang, Y. Ma and J. Yang, *Chem. Commun.*, 2020, **56**, 14685–14688.
- H. Xu, J. Wu, W. Luo, Q. Li, W. Zhang and J. Yang, *Small*, 2020, **16**, 2001775.
- W. J. Sun, H. Q. Ji, L. X. Li, H. Y. Zhang, Z. K. Wang, J. H. He and J. M. Lu, *Angew. Chem., Int. Ed.*, 2021, **60**, 22933–22939.
- G. Chen, Y. Yuan, H. Jiang, S. Ren, L. Ding, L. Ma, T. Wu, J. Lu and H. Wang, *Nat. Energy*, 2020, **5**, 605–613.
- Y. Lan, J. Chen, H. Zhang, W. Zhang and J. Yang, *J. Mater. Chem. A*, 2020, **8**, 15853–15863.
- J. Gao, N. Shi, X. Guo, Y. Li, X. Bi, Y. Qi, J. Guan and B. Jiang, *Environ. Sci. Technol.*, 2021, **55**, 10684–10694.
- Y. Guo, R. Zhang, S. Zhang, Y. Zhao, Q. Yang, Z. Huang, B. Dong and C. Zhi, *Energy Environ. Sci.*, 2021, **14**, 3938–3944.
- H. Liu, X. Lang, C. Zhu, J. Timoshenko, M. Ruscher, L. Bai, N. Guijarro, H. Yin, Y. Peng, J. Li, Z. Liu, W. Wang, B. R. Cuenya and J. Luo, *Angew. Chem., Int. Ed.*, 2022, e202202556.
- D. Wang and X. Gong, *Nat. Commun.*, 2021, **12**, 158.
- Z. Xue, H. Su, Q. Yu, B. Zhang, H. Wang, X. Li and J. Chen, *Adv. Energy Mater.*, 2017, **7**, 1602355.



- 25 J. Hou, Y. Sun, Y. Wu, S. Cao and L. Sun, *Adv. Funct. Mater.*, 2018, **28**, 1704447.
- 26 H. Su, K. Zhang, B. Zhang, H. Wang, Q. Yu, X. Li, M. Antonietti and J. Chen, *J. Am. Chem. Soc.*, 2017, **139**, 811–818.
- 27 H. Wang, Q. Mao, T. Ren, T. Zhou, K. Deng, Z. Wang, X. Li, Y. Xu and L. Wang, *ACS Appl. Mater. Interfaces*, 2021, **13**, 44733–44741.
- 28 R. Zhang, Y. Guo, S. Zhang, D. Chen, Y. Zhao, Z. Huang, L. Ma, P. Li, Q. Yang, G. Liang and C. Zhi, *Adv. Energy Mater.*, 2022, 2103872.
- 29 W. Teng, N. Bai, Y. Liu, Y. Liu, J. Fan and W. Zhang, *Environ. Sci. Technol.*, 2018, **52**, 230–236.
- 30 Y. Yu, C. Wang, Y. Yu, Y. Wang and B. Zhang, *Sci. China: Chem.*, 2020, **63**, 1469–1476.
- 31 P. Gao, Z. H. Xue, S. N. Zhang, D. Xu, G. Y. Zhai, Q. Y. Li, J. S. Chen and X. H. Li, *Angew. Chem., Int. Ed.*, 2021, **60**, 20711–20716.
- 32 X. Wan, W. Guo, X. Dong, H. Wu, X. Sun, M. Chu, S. Han, J. Zhai, W. Xia, S. Jia, M. He and B. Han, *Green Chem.*, 2022, **24**, 1090–1095.
- 33 J. Wang, C. Cai, Y. Wang, X. Yang, D. Wu, Y. Zhu, M. Li, M. Gu and M. Shao, *ACS Catal.*, 2021, **11**, 15135–15140.
- 34 X. Zhang, C. Wang, Y. Guo, B. Zhang, Y. Wang and Y. F. Yu, *J. Mater. Chem. A*, 2022, **10**, 6448–6453.
- 35 X. Li, W. Fan, Y. Bai, Y. Liu, F. Wang, H. Bai and W. Shi, *Chem. Eng. J.*, 2022, **433**, 133225.
- 36 R. Jia, Y. Wang, C. Wang, Y. Ling, Y. Yu and B. Zhang, *ACS Catal.*, 2020, **10**, 3533–3540.
- 37 Y. T. Wang, H. J. Li, W. Zhou, X. Zhang, B. Zhang and Y. F. Yu, *Angew. Chem., Int. Ed.*, 2022, e202202604.
- 38 X. Zhang, Y. Wang, C. Liu, Y. Yu, S. Lu and B. Zhang, *Chem. Eng. J.*, 2021, **403**, 126269.
- 39 X. Fu, C. Shang, G. Zhou and X. Wang, *J. Mater. Chem. A*, 2021, **9**, 24963–24970.
- 40 Q. Li, W. Deng, C. Li, Q. Sun, F. Huang, Y. Zhao and S. Li, *ACS Appl. Mater. Interfaces*, 2018, **10**, 40265–40273.
- 41 Y. Wang, W. Zhou, R. Jia, Y. Yu and B. Zhang, *Angew. Chem., Int. Ed.*, 2020, **59**, 5350–5354.
- 42 M. Li, C. Liu, Z. Zhang, S. Cao, H. Liu, S. Shen and W. Wang, *Sep. Purif. Technol.*, 2022, **281**, 119978.
- 43 W. Liu, Z. Zhang, Y. Zhang, Y. Zheng, N. Liu, J. Su and Y. Gao, *Nano-Micro Lett.*, 2021, **13**, 61.
- 44 X. Meng, Y. Xu, X. Sun, L. Xiong and Q. Wang, *J. Power Sources*, 2016, **326**, 389–396.
- 45 C. F. Yang, W. D. Zhong, K. Shen, Q. Zhang, R. Zhao, H. Xiang, J. Wu, X. K. Li and N. J. Yang, *Adv. Energy Mater.*, 2022, 2200077.
- 46 P. Ling, Q. Zhang, T. Cao and F. Gao, *Angew. Chem., Int. Ed.*, 2018, **57**, 6819–6824.
- 47 W. He, J. Zhang, S. Dieckhofer, S. Varhade, A. C. Brix, A. Lielpetere, S. Seisel, J. R. C. Junqueira and W. Schuhmann, *Nat. Commun.*, 2022, **13**, 1129.
- 48 M. Tahir, L. Pan, R. Zhang, Y. Wang, G. Shen, I. Aslam, M. A. Qadeer, N. Mahmood, W. Xu, L. Wang, X. Zhang and J. Zou, *ACS Energy Lett.*, 2017, **2**, 2177–2182.
- 49 Y. Lu, C. Dong, Y. Huang, Y. Zou, Y. Liu, Y. Li, N. Zhang, W. Chen, L. Zhou, H. Lin and S. Wang, *Sci. China: Chem.*, 2020, **63**, 980–986.
- 50 Z. Ping, Q. Sun, J. Yi, Q. Li, L. Zhao, H. Zhang, F. Huang, S. Li and L. Cheng, *ACS Appl. Mater. Interfaces*, 2021, **13**, 49556–49566.
- 51 X. Yu, B. Kim and Y. K. Kim, *ACS Catal.*, 2013, **3**, 2479–2486.
- 52 K. Qian, Y. Yan, S. Xi, T. Wei, Y. Dai, X. Yan, H. Kobayashi, S. Wang, W. Liu and R. Li, *Small*, 2021, **17**, 2102970.
- 53 S. Ye, Z. Chen, G. Zhang, W. Chen, C. Peng, X. Yang, L. Zheng, Y. Li, X. Ren, H. Cao, D. Xue, J. Qiu, Q. Zhang and J. Liu, *Energy Environ. Sci.*, 2022, **15**, 760–770.
- 54 C. Lv, L. Zhong, H. Liu, Z. Fang, C. Yan, M. Chen, Y. Kong, C. Lee, D. Liu, S. Li, J. Liu, L. Song, G. Chen, Q. Yan and G. Yu, *Nat. Sustain.*, 2021, **4**, 868–876.
- 55 Z. Wu, M. Karamad, X. Yong, Q. Huang, D. Cullen, P. Zhu, C. Xia, Q. Xiao, M. Shakouri, F. Chen, J. Y. T. Kim, Y. Xia, K. Heck, Y. Hu, M. Wong, Q. Li, I. Gates, S. Siahrostami and H. Wang, *Nat. Commun.*, 2021, **12**, 2870.
- 56 S. Z. Andersen, V. Colic, S. Yang, J. A. Schwalbe, A. C. Nielander, J. M. McEnaney, K. Enemark-Rasmussen, J. G. Baker, A. R. Singh, B. A. Rohr, M. J. Statt, S. J. Blair, S. Mezzavilla, J. Kibsgaard, P. C. K. Vesborg, M. Cargnello, S. F. Bent, T. F. Jaramillo, I. E. L. Stephens, J. K. Nørskov and I. Chorkendorff, *Nature*, 2019, **570**, 504–508.
- 57 L. Zhang, L. Ding, G. Chen, X. Yang and H. Wang, *Angew. Chem., Int. Ed.*, 2019, **58**, 2612–2616.
- 58 X. Yang, J. Nash, J. Anibal, M. Dunwell, S. Kattel, E. Stavitski, K. Attenkofer, J. Chen, Y. Yan and B. Xu, *J. Am. Chem. Soc.*, 2018, **140**, 13387–13391.
- 59 C. Hu, X. Chen, J. Jin, Y. Han, S. Chen, H. Ju, J. Cai, Y. Qiu, C. Gao, C. Wang, Z. Qi, R. Long, L. Song, Z. Liu and Y. Xiong, *J. Am. Chem. Soc.*, 2019, **141**, 7807–7814.
- 60 J. S. Zhu, H. Yang, W. H. Zhang, Y. C. Mao, S. S. Lyu and J. Chen, *Inorg. Chem. Front.*, 2020, **7**, 1892–1899.
- 61 D. P. Butcher Jr. and A. A. Gewirth, *Nano Energy*, 2016, **29**, 457–465.
- 62 F. Lei, K. Li, M. Yang, J. Yu, M. Xu, Y. Zhang, J. Xie, P. Hao, G. Cui and B. Tang, *Inorg. Chem. Front.*, 2022, **9**, 2734–2740.
- 63 S. H. Han, S.-i Jeon, J. Lee, J. Ahn, C. Lee, J. Lee and J. Y. Yoon, *Chem. Eng. J.*, 2022, **431**, 134233.
- 64 Y. X. Guo, J. R. Stroka, B. Kandemir, C. E. Dickerson and K. L. Bren, *J. Am. Chem. Soc.*, 2018, **140**, 16888–16892.

